Gravity waves generated by deep tropical convection: Estimates from balloon observations and mesoscale simulations

Valérian Jewtoukoff,[1] Riwal Plougonven,[2] and Albert Hertzog[2]

[1]   Convective gravity waves in the Tropics are studied by analyzing in situ measurements from long-duration stratospheric balloons launched during the PreConcordiasi campaign (2010) and mesoscale simulations. An improved temporal resolution of the observations as well as the balloon quasi-Lagrangian behavior allow an unprecedented investigation of the whole gravity wave spectrum. First, a case study of gravity waves generated by a developing cyclone, Tropical Storm Gelane (February 2010), is carried out using observations complemented by numerical simulations with the Weather Research and Forecast model, with a resolution down to 1 km. Distributions of momentum fluxes obtained from both data show reasonable agreement and emphasize waves with short wavelengths (< 15 km) and short periods (< 20 min). Still, some differences are also found, which can likely be related to errors of the modeled background flow. Second, observations from the whole PreConcordiasi flights are analyzed with an emphasis on gravity wave momentum fluxes. Their phase speed distribution has a robust shape, with maximum fluxes with near-zero ground-based phase speeds. Yet, significant momentum fluxes are also found for larger values, yielding a mean phase speed of about 27 m s^{-1}. The momentum fluxes are concentrated in short episodes with intense values, and their intermittency is quantified using probability distribution functions and the Gini coefficient (0.5–0.6). The relative importance of convective and topographic sources are investigated, suggesting comparable intensities, but a greater occurrence frequency of convective events. Waves emitted by Tropical Storm Gelane do not stand out relative to other convective events.

Citation: Jewtoukoff, V., R. Plougonven, and A. Hertzog (2013), Gravity waves generated by deep tropical convection: Estimates from balloon observations and mesoscale simulations, *J. Geophys. Res. Atmos.*, *118*, 9690–9707, doi:10.1002/jgrd.50781.

1. Introduction

[2] Gravity waves (GW) are key processes in the global middle atmosphere circulation. Their momentum, which is transported upward from tropospheric sources, is deposited in the stratosphere and mesosphere and essentially contributes to the force balance at those altitudes [*Fritts and Alexander*, 2003]. In the midlatitudes, GWs are consequently involved in the maintenance of the Brewer-Dobson circulation [*Holton et al.*, 1995], and they play a major role as well in driving the Quasi-Biennial Oscillation in the tropics [*Dunkerton*, 1997; *Kawatani et al.*, 2010; *Evan et al.*, 2012]. Since they occur on relatively small scales (∼10–1000 km in the horizontal; some kilometers at most in the vertical), dedicated parameterizations are needed to simulate their effects in atmospheric Global Circulation Models (GCMs) [*Kim et al.*, 2003]. Deficiencies in these parameterizations, and in particular in those used for nonorographic GWs, have been and remain a significant contributor to the biases of the so-called high-top GCMs, i.e., those including a well-resolved stratosphere [*Pawson et al.*, 2000; *Austin et al.*, 2003; *Butchart et al.*, 2010]. These deficiencies constitute a great motivation for improving our knowledge and understanding of atmospheric gravity waves, both through observations and numerical modeling [*Alexander et al.*, 2010].

[3] Deep convection is known to be one of the main sources of nonorographic GWs in the tropics, as evidenced in global maps of momentum fluxes obtained from satellite observations [e.g., *Ern et al.*, 2011]. Convectively generated gravity waves (CGW) have been the focus of observational studies using airborne measurements [e.g., *Pfister et al.*, 1993; *Wang et al.*, 2006], radar measurements [e.g., *Sato*, 1993], and satellite observations [e.g., *Dewan et al.*, 1998]. These studies have highlighted the importance of waves with horizontal scales of tens to hundreds of kilometers and vertical scales of about 10 km, corresponding to short intrinsic periods (i.e., a few tens of minutes).

[1]Laboratoire de Météorologie Dynamique du CNRS, Ecole Normale Supérieure, Paris, France.
[2]Laboratoire de Météorologie Dynamique du CNRS, Ecole Polytechnique, Palaiseau, France.

Corresponding author: V. Jewtoukoff, Laboratoire de Météorologie Dynamique du CNRS, Ecole Normale Supérieure, 24 rue Lhomond, 75005 Paris, France. (vjewtou@lmd.ens.fr)

[4] Among convective sources, Tropical Cyclones stand out as intense, organized events and have been specifically studied for their generation of GWs, both with observations [e.g., *Sato*, 1993; *Dhaka et al.*, 2003] and with numerical simulations [*Kim et al.*, 2005, 2007; *Kuester et al.*, 2008; *Kim and Chun*, 2010]. As finer resolution has become available, numerical simulations have stressed the role of waves with shorter and shorter wavelengths: *Kim et al.* [2005] simulated waves emitted by typhoon Rusa (2002) with a horizontal resolution of $\Delta x = 27$ km and found dominant wavelengths of 300–600 km, with periods of 6–11 h. *Kuester et al.* [2008] simulated Hurricane Humberto (2001) with a resolution down to $\Delta x = 3$ km and found dominant wavelengths of 15–300 km, with periods 20–100 min. Similarly, *Kim and Chun* [2010] simulated waves emitted by Typhoon Saomai (2006) and found dominant wavelengths of 10–100 km, with periods less than 2 h. These different studies have consistently contrasted the emission during different cyclone stages, showing stronger emission and shorter wave scales during the development stage as compared to later stages [*Kuester et al.*, 2008; *Kim and Chun*, 2010]. Phase speeds have been found to be mostly eastward, with typical values around 20 to 30 m s^{-1}. Local maxima of momentum fluxes have been estimated from observations as ~ 40 mPa [*Sato*, 1993] and similar values from simulations (10–30 mPa in *Kuester et al.* [2008], 30–50 mPa in *Kim and Chun* [2010]). *Kim and Chun* [2010] improved on previous simulations by the extent of the fine-resolution domain. They displayed significant sensitivity of the model results to the resolution. In fact, at resolutions that are presently available for three-dimensional simulations, it is expected that CGWs will remain sensitive to resolution [*Lane and Knievel*, 2005]. In this respect, it is all the more important to have an observational counterpart to the numerical simulations. However, the short horizontal scales and high temporal frequencies of gravity waves generated by convection, as well as their location in the vicinity of cyclones, constitute major difficulties for many observing techniques. Recent long-duration balloon observations performed with a sampling frequency sufficient to resolve the whole GW spectrum provide a unique opportunity for such a comparison.

[5] Balloon-borne observations have already been used to estimate gravity wave momentum fluxes, either in the tropics [*Hertzog and Vial*, 2001] or at high latitudes [*Vincent et al.*, 2007; *Hertzog et al.*, 2008], and have also been successfully compared to high-resolution numerical simulations [*Plougonven et al.*, 2008, 2013]. They also served to describe gravity wave intermittency [*Alexander et al.*, 2010; *Hertzog et al.*, 2012], which is arguably a characteristic feature of convection. One outstanding characteristic of long-duration balloons is that they move with the wind, so that the intrinsic frequency ($\hat{\omega}$) of gravity wave packets are directly inferred from the observations. In these previous studies, however, the sampling rate during the flights, 1 obs/15 min, was too slow to resolve most of the waves generated by convection. Recently, the baud rate of the space link used to transfer data to the ground was increased so that it became possible to perform observations every 30 s during the flights, increasing the sampling rate by a factor 30. Consequently, the whole gravity wave spectrum ($|f| \leq \hat{\omega} \leq N$, with f and N the inertial and Brunt-Väisälä frequencies, respectively) is resolved in these observations. Three recent

long-duration superpressure balloons (SPB) launched from Seychelles Islands in 2010 in the framework of the PreConcordiasi campaign will be used here and provide the basis for the comparisons with numerical simulations of CGWs.

[6] The present study is divided into two distinct parts: In the first part, we focus on a case study where balloon observations have been collected over a developing cyclone in the Indian Ocean. Numerical simulations are specifically designed to reproduce this case, so as to let us compare the characteristics of simulated CGWs with those derived from the balloon observations. In the second part, we analyze GW signatures during the whole three balloon flights and aim at assessing the representativity and contribution of GW generated by Tropical Storms and Tropical Cyclones in the whole tropical belt.

[7] The paper is organized as follows: The balloon campaign, observations, and analysis method are first presented in section 2. The case study of the developing cyclone is described in section 3, as well as the associated numerical simulations. The characteristics of the observed and simulated gravity waves corresponding to this event are quantified and compared in section 4, while section 5 presents the observed overall wave characteristics for the whole three balloon flights. A summary and conclusion are presented in the last section.

2. Balloon Observations

2.1. The PreConcordiasi Campaign

[8] During the preparation of the Concordiasi campaign [*Rabier et al.*, 2010], the French Space Agency (Centre National d'Etudes Spatiales (CNES)) released three SPBs from Mahe Airport (55.530°E, 4.679°S), Seychelles Islands in February 2010. SPBs are closed balloons filled with helium, which drift on constant-density surface in the atmosphere [*Hertzog et al.*, 2007]. The PreConcordiasi flights were aimed at testing the balloons and payloads designed for Concordiasi. In particular, they hosted the Thermodynamic SENsor (TSEN) meteorological package that performs in situ observations of pressure and temperature along the flights. The wind is deduced from the successive balloon positions provided by a GPS receiver onboard the CNES main gondola, as during previous campaigns.

[9] The balloons flew in the lower tropical stratosphere between typically 19 and 20 km altitude ($\sim$ 55–65 hPa) (see flight-mean statistics in Table 1). The flight trajectories are displayed on Figure 1. During the campaign, the quasi-biennial oscillation (QBO) in the stratospheric equatorial winds reverses at the flight level of the balloons, inducing eastward zonal wind at the beginning of the flight period and westward wind at the end. For some periods, in particular, the QBO signal was weak enough so that the balloons were very sensitive to the residual seasonal cycle and to any wind disturbance (e.g., Rossby-gravity or inertial waves) present in the equatorial lower stratosphere at that time. As a consequence, the balloon trajectories were relatively complicated. Balloon #1 for instance stayed some days over the Indian Ocean close to the Seychelles Islands before being advected over Africa. It was then embedded in the QBO eastward circulation and, respectively, crossed the Indian and Pacific Ocean before experiencing the QBO reversal and flying back

Table 1. PreConcordiasi Balloon Flights

				Flight-Mean Statistics		
Flight	Launch (dd/mm/yyyy)	End (dd/mm/yyyy)	Duration (day)	Altitude (km)	Pressure (hPa)	Density (kg/m³)
1	8/2/2010	11/5/2010	92	19.8	59.4	0.103
2	19/2/2010	8/5/2010	79	19.3	64.2	0.114
3	21/2/2010	12/5/2010	81	19.6	61.2	0.114

over the Pacific Ocean. The flight ended 3 months after the launch in the South China Sea, northwest of Borneo. Like balloon #1, balloon #2 stayed in the deep tropics. It first made a complete eastward revolution around the Earth and then flew back over the Indian Ocean where the flight ended. Balloon #3 on the other hand drifted southwestwardly toward the subtropics, so that it eventually became advected by the developing midlatitude westerlies of the southern winter.

2.2. Estimation of Gravity Wave Characteristics From the Balloon Observations

[10] In this study, we will essentially use the equations and methodology developed in *Boccara et al.* [2008] to estimate gravity wave momentum fluxes and phase speeds from long-duration balloon observations. Briefly, a (complex) wavelet analysis is used to decompose the observed time series of pressure, wind, and vertical displacement in the time-intrinsic frequency space, and the resulting wavelet coefficients are combined to retrieve the wave packet characteristics. However, as recalled in section 1, this former study essentially dealt with hydrostatic waves ($\hat{\omega} \ll N$), in contrast with what is sought here. A few adjustments were therefore needed to analyze the PreConcordiasi flights, regarding high-frequency oscillations, the estimation of phase speeds, and periods of depressurization, as detailed below.

[11] We must first ensure that the balloon's neutral oscillations about its equilibrium level do not interfere with the gravity wave signals. The pulsation of the balloon oscillations can be theoretically derived by assuming that a fully pressurized balloon keeps its volume constant during these motions (and thus its density too). At first order, the balloon vertical displacement (δz) simply responds to the buoyant forces:

$$\frac{d^2 \delta z}{dt^2} = -g \frac{\rho_b - \rho}{\rho} \tag{1}$$

where g is the Earth's gravity, ρ_b is the balloon density, and ρ is the atmospheric density. Using the perfect gas law to relate the vertical variation of the atmospheric density to those of temperature (T) and pressure (P), and with the help of the hydrostatic equilibrium, one obtains

$$\frac{d^2 \delta z}{dt^2} + \omega_b^2 \delta z = 0 \tag{2}$$

where

$$\omega_b = \sqrt{\frac{g}{T}\left(\frac{\partial T}{\partial z} + \frac{g}{R}\right)} \tag{3}$$

is the angular frequency of the balloon oscillations. In this equation, R is the perfect gas constant per mass unit of air.

The balloon neutral oscillations therefore occur with a higher frequency than the Brunt-Väisälä frequency

$$N = \sqrt{\frac{g}{T}\left(\frac{\partial T}{\partial z} + \frac{g}{C_p}\right)}.$$

Taking a mean value for the vertical gradient of temperature in the lower equatorial stratosphere of 5 K km⁻¹ yields $2\pi/\omega_b \sim 2.5$ min. Observations show that the real balloon oscillations are slightly longer, which mainly results from the balloon convecting some air with it during its displacement [*Nastrom*, 1980]. Yet these periods are still shorter than those of the shortest gravity waves in the intrinsic frame of reference (4 min), and the associated signals can thus be essentially separated from the gravity wave ones in the wavelet analysis that we perform to infer the wave characteristics.

[12] In this study, intrinsic phase speeds of gravity wave packets ($\hat{c}$) are directly inferred from equation (6) in *Boccara et al.* [2008] as:

$$\hat{c} = \frac{1}{\bar{\rho}\delta_-} \frac{Re(u'_\parallel p'^\star_w)}{u'^2_\parallel} \tag{4}$$

with $\bar{\rho}$ denoting the mean density along the flight, $\delta_- = 1 - f^2/\hat{\omega}^2$, p'_w and $u'_\parallel$, respectively, denoting the complex wavelet coefficients for the Eulerian pressure disturbance and for the wind disturbance in the wave direction of propagation, and $p'^\star_w$ denoting the complex conjugate of p'_w. The Eulerian pressure disturbance is inferred from the observed Lagrangian pressure disturbance (p'_l):

$$p'_w = p'_l + \bar{\rho}g\zeta'_b \tag{5}$$

where the balloon vertical displacement (ζ'_b) is obtained from the embarked GPS. This phase speed estimation from the Eulerian pressure perturbation is rendered possible thanks to a 1 order of magnitude improvement in the precision of GPS altitudes (1.5 m for the 2010 flights versus 15 m previously).
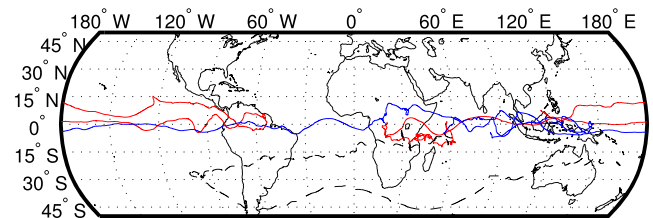

Figure 1. Trajectory of balloon 1 (red), 2 (blue), and 3 (dashed black) in the lower stratosphere during the PreConcordiasi campaign (February–May 2010).
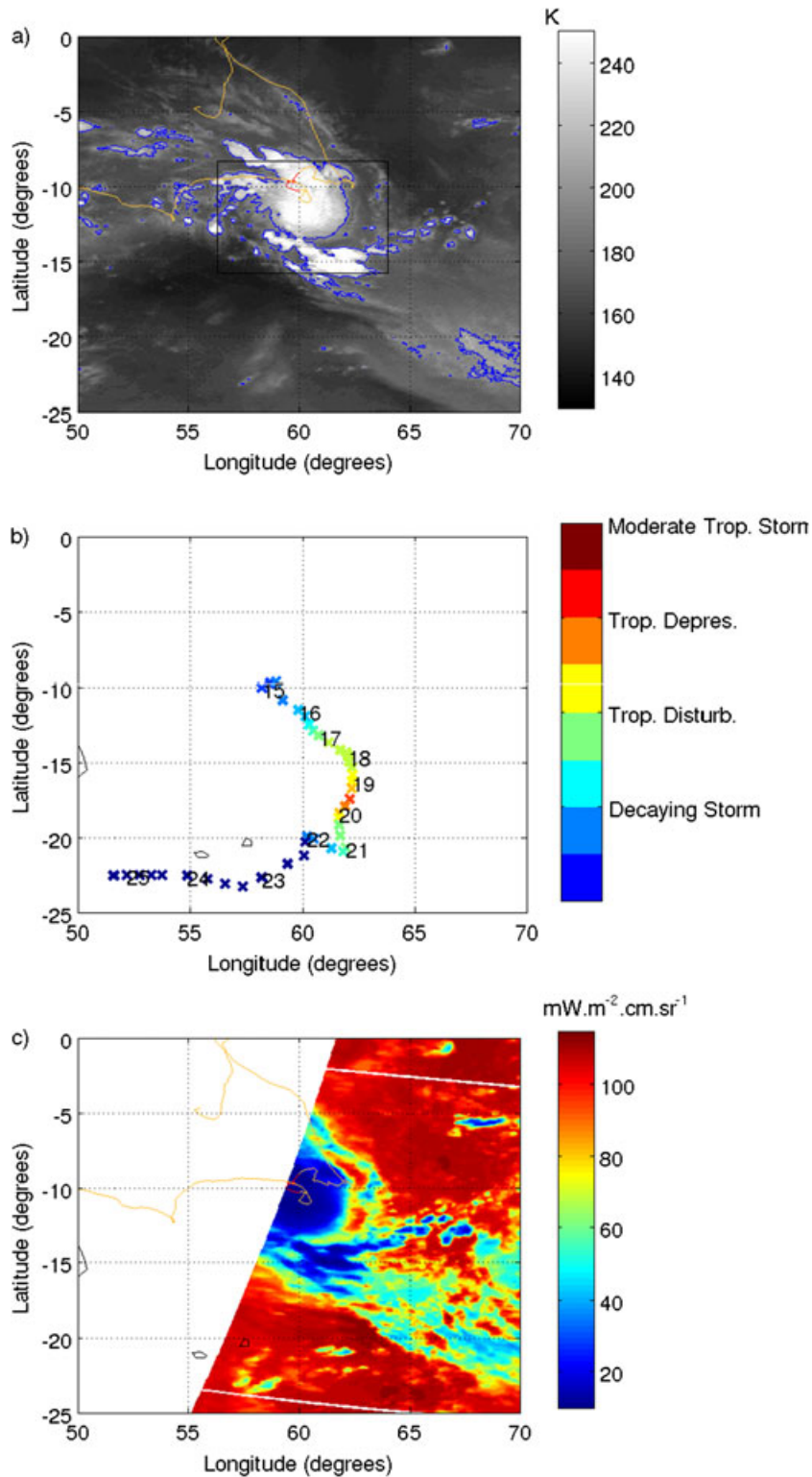
Figure 2. (a) Brightness temperatures in the Meteosat-6 water vapor channel on 15 February 2010 at 2200 UTC. The indicative contour at 200 K is represented in blue. The balloon trajectory on the 15 February 2010 is shown with the red curve, while the extended trajectory is denoted by the yellow curve. The black square corresponds to one of the domain used in the numerical simulation, later referred to as D03. (b) Tropical Cyclone Gelane track with the corresponding Southwest Indian Ocean Tropical Cyclone scale category and dates. (c) Atmospheric Infrared Sounder (AIRS) radiances at 2100 UTC for channel 763 (tropospheric channel), balloon trajectory during the 15 February 2010 (red line), and extended trajectory (yellow).

Table 2. Domain Setup

Domain	D01	D02	D03	D04
Grid dimension (x, y)	70×70	151×151	271×271	346×346
Horizontal resolution (km)	27	9	3	1
Vertical levels (z)	121	121	121	121
Integration time (UTC)	0000–2400	0000–2400	1800–2400	1800–2400
Output frequency (min)	30	30	30	1

Tests performed on synthetic time series including measurement noise have shown that the phase speeds are estimated with a 1-σ uncertainty of 9 m s^{-1}. The wave packet horizontal wavelengths are then obtained as $\lambda_h = 2\pi \hat{c}/\hat{\omega}$, and the vertical wavelengths are finally estimated from the gravity wave dispersion relation.

[13] Last, it is necessary to evaluate the impacts of balloon depressurization on the estimation of gravity wave characteristics. Specifically, the case study presented below occurred on 15–16 February 2010, when balloon #1 flew over the Intense Tropical Cyclone Gelane over the western Indian Ocean (see section 3). Besides disturbances in wind and pressure time series, this period is also characterized by a sudden drop of the balloon superpressure, which eventually vanishes for 15 h, between 1200 UTC on the fifteenth and 0300 UTC on the sixteenth. This depressurization event constitutes another difference with the previous work of *Boccara et al.* [2008]. During these periods, actually, the balloon density is no longer constant, since the balloon volume may vary. These periods typically occur when the balloons fly over areas of organized deep convection as the upward infrared flux impinging on the balloon envelope becomes very weak, cooling the lifting gas and consequently lowering its pressure. Now, the estimation of the gravity wave momentum fluxes in *Boccara et al.* [2008] relies on the balloon drifting on constant-density surfaces and may therefore be biased during depressurization events. The effect of depressurization events on the momentum flux estimates is assessed in Appendix A, where it is shown that momentum fluxes are likely overestimated during such periods, but with no more than a factor 2.

3. Overall Description of the Case Study

[14] We focus our case study on late 15 February 2012, during the early development stage of Tropical Cyclone Gelane. Balloon 1 flew over the main convective core of the Tropical Storm during that period (Figure 2a). The storm track and the corresponding Southwest Indian Ocean Tropical Cyclone scale category are represented on Figure 2b.

3.1. Meteorological Situation

[15] On 15 February 2010, Météo France announced the formation of Tropical Disturbance 12 approximately 1200 km northeast of La Réunion island. During the following hours, the storm continued to develop and drift south-southeasterly as deep convection concentrated vorticity near the core, was then classified as Moderate Tropical Storm, and renamed Gelane. Satellite observations of atmospheric water (Figure 2c) reveal that on 15 February 2010, episodic cellular convection occurred on the upshear side (eastern half) of the storm, in the core and outer bands. The storm intensified, reaching Severe Tropical Storm intensity on 17 February and becoming an Intense Tropical Cyclone on 18 February. When the system reached its peak intensity on 19 February, the minimum sea level pressure was 930 hPa at the core of the Cyclone. Then, finally, turning to the west and moving toward Madagascar, the remnants of Gelane quickly dissipated $\sim$ 200 km under the effects of the increasing vertical wind shear.

3.2. Model Setup

[16] We investigate the stratospheric gravity waves generated by this Tropical Storm through a numerical simulation with the Weather Research and Forecast (WRF) Model [*Skamarock et al.*, 2008]. WRF is a nonhydrostatic compressible mesoscale model well suited for studying convectively generated gravity waves. The horizontal grid uses Arakawa-C staggering, and the vertical coordinate is terrain following. Time integration uses a third-order scheme with small time steps for acoustic and gravity waves [*Wicker and Skamarock*, 2002].

[17] Two-way nesting is used to perform high-resolution model integrations (see Table 2). Hereafter, the domains with horizontal grid spacings of 27, 9, 3, and 1 km are referred to as D01, D02, D03, and D04, respectively. The domains are centered on 60°E, 10°S, which corresponds to

Table 3. Model Physics

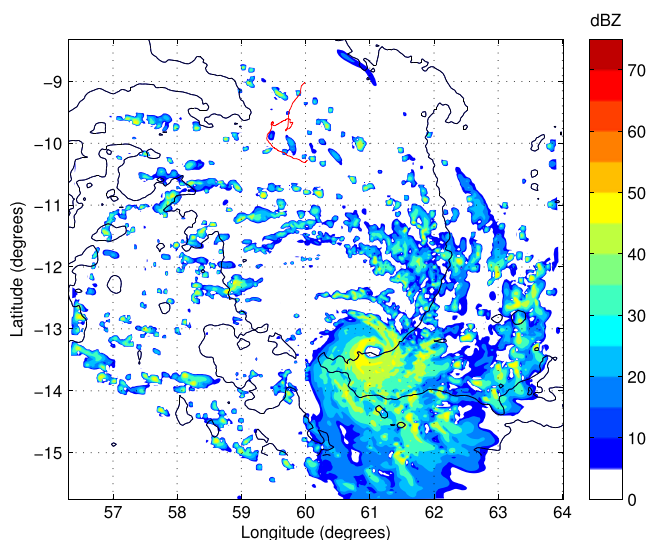| Model Physics	References
Morrison double-moment microphysics	*Morrison et al.* [2009]
Kain-Fritsch convective scheme	*Kain* [2004]
(for D01 and D02 only)	
Yonsei University planetary boundary layer scheme	*Hong and Pan* [1996]
MM5-derived surface layer scheme	*Skamarock et al.* [2005]
Noah land surface model	*Chen and Dudhia* [2001]
Rapid radiative transfer model for longwave radiation	*Mlawer et al.* [1997]
Dudhia shortwave radiation scheme	*Dudhia* [1989]

Figure 3. Simulated radar reflectivity in D03 at 2200 UTC and balloon trajectory on 15 February 2010 (red line). The overlaid black contour is the blue contour on Figure 2a and represents an estimation of the main convection system associated with Gelane as observed by Meteosat-6.

the mean location of the simulated storm core. This positioning was performed manually and was based on previous test simulations. From the coarser to the finer, the domains, respectively, have dimensions of 70 × 70, 151 × 151, 271 × 271, and 346 × 346 grid points. Each nested domain contains 120 vertical levels from the surface to the model top, chosen as 6 hPa and corresponding to an approximate altitude of 35 km. We prescribe a sponge layer effective in the upper 7.5 km below the domain top, using Rayleigh damping on the vertical velocity to avoid wave reflections on the model top. A few tests were necessary to determine the optimal thickness of this layer.

[18] The physical schemes are summarized in Table 3. For example, convection is explicitly simulated in D03 and D04 while it is parameterized in the two first domains using the Kain-Fritsch scheme [*Kain*, 2004]. This scheme showed good results when simulating Tropical Storms [*Gentry and Lackman*, 2006]. Moreover, we used the Morrison double-moment microphysics scheme because it includes graupel and ice and the associated processes necessary to simulate convection at cloud-scale.

[19] The reference simulation covers the 24 h period from 15 February 2010 at 0000 UTC to 16 February 2010 at 000 UTC. The model first ran on D01 and D02 until 1800 UTC; at which time, all four domains were run together for the last 6 h. In the rest of the study, we will focus on the period from 2030 to 2400 UTC (i.e., after the spin up of the flow in D03 and D04). The atmospheric initial conditions and boundary conditions for D01 were provided by the European Centre for Medium-Range Weather Forecasts (ECMWF) operational analyses. These analyses are available at 0000, 0006, 1200, and 1800 UTC every day. They have a horizontal resolution of 0.25° corresponding to an approximate grid spacing of 20–25 km, and 91 model levels in the vertical, with a higher resolution near the

surface. In addition, we have performed another run with D03 and D04 starting at 1200 UTC, in order to test the sensitivity to the model spin-up in those domains. Unless stated otherwise, we only discuss below results from the reference simulation.

[20] It was furthermore found necessary to carefully initialize the model run with data assimilation of satellite radiances complementing the information from the ECMWF analyses. Preliminary cold start initialization tests with data provided only by ECMWF did not successfully simulate the Tropical Cyclone (probably because of insufficient use of the complete set of fields by WRF, like the cloud liquid water, for example). Hence, satellite radiances from the NOAA Advanced Microwave Sounding Unit B (AMSU-B) [*Aumann et al.*, 2003; *Fetzer et al.*, 2003] before the run period were assimilated through intermittent assimilation cycles on the D01 grid to initialize the model with realistic convection. AMSU-B is a microwave radiometer onboard near-polar orbiting satellites, which measures the atmospheric humidity profile and complements the temperature sounding instruments AMSU-A and High-Resolution Infrared Radiation Sounder/3. The assimilation is performed with the WRF Data Assimilation 3DVAR package (WRFDA-3DVAR) [*Barker et al.*, 2004]. We perform the first 3DVAR assimilation cycle on 14 February at 0600 UTC, and then, cycle it every 6 h until 15 February at 0000 UTC. In contrast with numerous other studies focusing on Hurricane simulations, we therefore did not use a bogus vortex [*Singh et al.*, 2005] to force the circulation at the initial time. However, we note that assimilation of AMSU-B here was the key element to simulate convection comparable to that observed in the Meteosat-6 and AIRS data.

3.3. Simulated Storm and Model Validation

[21] Figure 3 shows the simulated radar reflectivity in D03 at 2200 UTC to identify deep moist convection associated to the developing Tropical Storm. The simulated storm shows the typical features of a real Tropical Storm, with converging winds near the surface (not shown), a cloud-free core, eye-wall clouds overshooting at an altitude of about 15 km, and spiraling rainbands, denoted by the strong reflectivity cores outside the storm core. Moreover, the simulated values of 35 dBZ with maxima of 55 dBZ are typical values of radar reflectivity for Tropical Storms and Tropical Cyclones. For comparison, those values are usually between 55 and 70 dBZ in classical monocellular or multicellular convective storms.

[22] In D01, the Tropical Storm intensifies slowly immediately after the beginning of the run and starts to drift south-southeasterly with a speed of 5 m s^{-1}. In D02, D03, and D04, the Tropical Storm intensifies more rapidly than observed by Météo France and already reaches Severe Tropical Storm intensity by the end of 15 February. The Storm speed of displacement is realistic and appears to be of the same order than that of the real storm. Nonetheless, the simulated core is located 100–150 km south-southeasterly of its observed location. Cyclone trajectories are notoriously difficult to predict [e.g., *Plu*, 2011, and references therein], and this should not hinder the comparison below. The position and characteristics of the storm remain essentially unchanged in the simulation with the longer spin-up for D03 and D04.
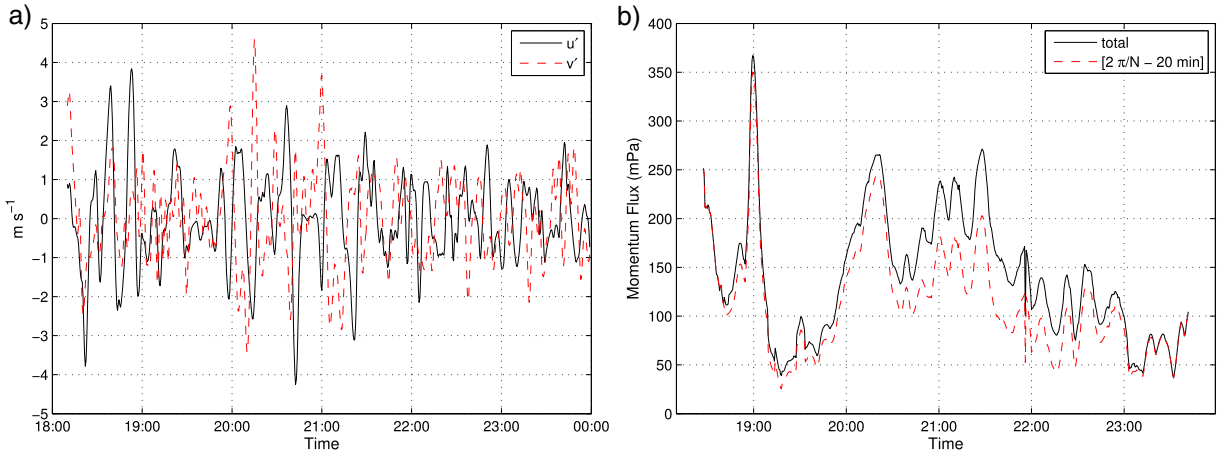
Figure 4. (a) u' (black) and v' (dashed red) perturbation velocities time series as measured by the first balloon on 15 February 2010. (b) Instantaneous momentum flux computed using the first balloon data during the Tropical Storm phase (solid black). We have represented the contribution of CGWs with $\hat{T} = [2\pi/N, 20 \text{ min}]$ by the dashed red line.

4. Gravity Waves Associated With Gelane Tropical Storm

4.1. Estimates From the Balloon Observations

[23] In what follows, in order to compare the simulation with the balloon observations, we provide a first estimate of the CGW characteristics from a straightforward graphical analysis of the balloon time series. A more quantitative analysis, using wavelets, is presented afterward. In contrast to *Plougonven et al.* [2008], which investigated a single orographic wave, making pointwise comparisons possible, here we aim at deriving the typical amplitudes and characteristics of multiple wave packets.

4.1.1. Description of the Waves in the Balloon Observations

[24] Time series of zonal (u') and meridional (v') wind perturbations observed by balloon #1 on 15 February 2010 are displayed on Figure 4a. They have been obtained by filtering the raw time series with a band-pass filter with cutoff periods at 5 min and 24 h. The filtered time series exhibit disturbances with intrinsic periods ($2\pi/\hat{\omega}$) around 10–12 min, i.e., slightly more than twice the Brunt-Väisälä period, therefore indicative of gravity waves. As in *Plougonven et al.* [2008], an analysis of the characteristics of the waves in the balloon observations is now done with the help of the polarization and dispersion relations for gravity waves. We use standard notations and decompose the perturbation fields a' into monochromatic plane waves:

$$a' = \text{Re}\left(\tilde{a} e^{i(kx+ly+mz-\omega t)}\right) \quad (6)$$

where Re stands for the real part, $\tilde{a}$ is the complex amplitude of a', (k, l, m) are the zonal, longitudinal, and vertical wave numbers, and ω is the definite positive absolute frequency. With a Coriolis parameter nearly vanishing in the deep tropics, the polarization relations for 2-D linearly polarized gravity wave read [*Fritts and Alexander*, 2003; *Plougonven et al.*, 2008]:

$$\tilde{u} = \frac{k}{l}\tilde{v} \quad (7)$$

$$\tilde{w} = \frac{m\hat{\omega}}{N^2 - \hat{\omega}^2}\tilde{p} \quad (8)$$

$$\tilde{\zeta} = -i\frac{\hat{\omega}}{N^2}\frac{m}{k}\tilde{u} \quad (9)$$

where ($\tilde{u}, \tilde{v}, \tilde{w}, \tilde{\zeta}$), respectively, stand for the complex amplitudes of the velocity perturbations in the zonal, longitudinal, and vertical directions, and of the height perturbations. Here the terms involving the scale height H in *Fritts and Alexander* [2003] are neglected because the vertical wavelengths, of typically the order of the diabatic heating scale, i.e., ~ 10 km, are assumed to be small with respect to $4\pi H$.

[25] It is possible to estimate the wave propagation direction k/l in the horizontal plane using equation (7) and the series of u' and v' for the considered period. Throughout the considered period, calculated values of the counterclockwise angle from the East are found within a range from $\sim 0°$ at 1800 UTC to $\sim -60°$ from 2000 to 2400 UTC. Furthermore, following equation (7), the horizontal compo-
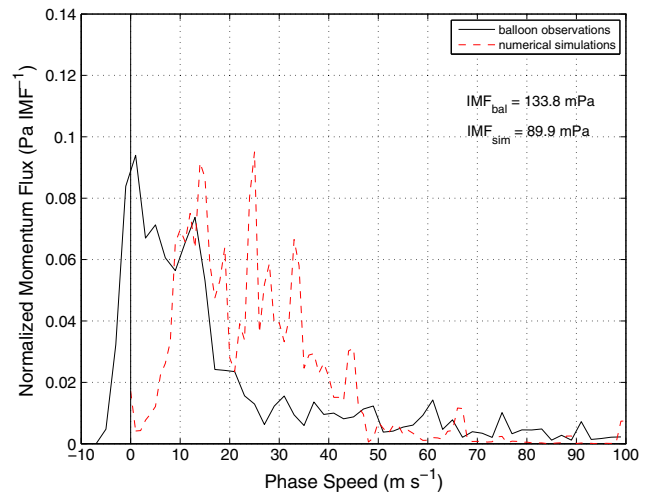

Figure 5. Ground-relative phase speeds associated with convective gravity waves in the balloon observations (black solid) and in the simulation (dashed red).
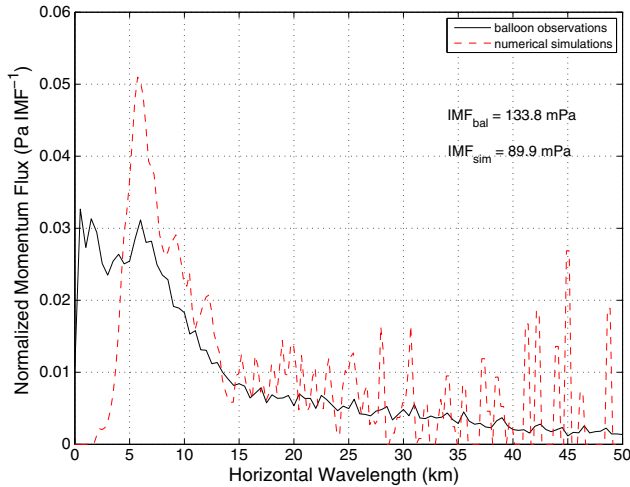
Figure 6. Horizontal wavelength spectra associated with convective gravity waves in the balloon observations (black solid) and in the simulation (dashed red).

nents of the velocity perturbations are in phase opposition, and this is observed in the time series of Figure 4 between 2000 and 2130 UTC, for example. Calculating a typical squared Brunt-Väisälä frequency of 7.5×10^{-4} s^{-2} (period of $\sim$ 4 min) from the ECMWF reanalysis along the balloon trajectory, and using equation (8) and w' and p' time series (not shown), we can estimate a typical vertical wavelength as $\lambda_z \sim 6$ km. Finally, we retrieve a horizontal wave number by using the dispersion relation:

$$\hat{\omega}^2 = \frac{N^2 k_H^2}{k_H^2 + m^2} \qquad (10)$$

with $k_H^2 = k^2 + l^2$. We find a value of 6.4×10^{-4} m^{-1}, yielding an horizontal wavelength of $\sim$ 10 km. Using equation (9) and considering the period when the propagation angle is constant and $\sim$ –60° (i.e., past 2000 UTC), we can finally calculate a typical height perturbation amplitude $\tilde{\zeta} \sim 200$ m.

4.1.2. Wavelet Analysis of the Balloon Data

[26] After the preliminary estimate of wave characteristics described above, we now carry out a systematic examination of the waves using wavelet analysis (section 2.2 and Appendix A) which provides estimates of the momentum fluxes, of phase speeds, frequencies, and wavelengths.

[27] The time series of the absolute momentum fluxes due to gravity waves obtained from the balloons with the wavelet analysis are shown in Figure 4b (solid black line). We note strong variations on timescales less than an hour with peaks exceeding 150 mPa.

[28] The wavelet analysis identifies wave packets and provides estimates of their intrinsic frequency. In order to quantify the contribution of high-frequency gravity waves to the total instantaneous momentum flux, we also show in Figure 4b the contribution of the waves with intrinsic periods shorter than 20 min (dashed red line). This clearly shows that most of the momentum flux (about 80%) is carried by the gravity waves with highest intrinsic frequencies.

[29] The wavelet analysis also provides estimates of the waves phase speeds and wavelengths. This information is used to describe the gravity wave momentum fluxes as a function of phase speed and horizontal wavelength, with bins of respective width $\Delta c = 2$ m s^{-1} and $\Delta\lambda_H = 500$ m. The ground-based phase speeds and horizontal wavelengths spectra of momentum fluxes are displayed in Figures 5 and 6 (solid black lines). The major part of momentum fluxes is accounted for by waves with phase speeds within a range of 0 to 50 m s^{-1}, and horizontal wavelengths within a range of 1 to 50 km. Both momentum flux distributions have two modes. The characteristics of the mode that carries the most momentum flux are summarized in Table 4 for comparison with the numerical simulations. These characteristics are in fair agreement with the first estimates provided in the previous section, both emphasizing short horizontal wavelengths: $\lambda_H \lesssim 10$ km.

4.2. Simulated Gravity Waves

[30] We now turn to the numerical simulations and aim at comparing the gravity waves emitted by Gelane in the simulations with those derived from the balloon observations.

4.2.1. Description of the Waves in the Numerical Simulation

[31] In this section, we first describe the simulated waves in physical space, relative to the large-scale flow structure, then examine their characteristics as a function of phase speeds and wavelengths.

[32] In Figure 7, we have represented horizontal cross sections of the vertical wind velocity and horizontal velocity vector at 2030 and 2210 UTC, 15 February 2010 in D04 at 7 and 19 km, the latter corresponding to the mean altitude of the balloon during the storm period. Figures obtained from the simulation with a longer spin-up for D03 and D04 are very similar. Whereas in the troposphere, the signature in vertical velocity is fairly isotropic; in the lower stratosphere, we clearly see the main gravity waves east of the core, located in a region delimited by 12.5°S, 13.5°S, and 60.5°E–61.5°E and also a small region northwest of the core. We notice a wavefront propagating away radially from the wall cloud around the core at a speed of 25 m s^{-1} on the eastern half side of the storm, surrounded by wave packets with smaller amplitude and horizontal scale. The majority of the waves propagate against the mean easterly flow. This result is consistent with previous theoretical studies on the propagation of gravity waves in sheared flows [*Beres et al.*, 2002]. A graphical estimation of the typical horizontal wavelengths yields $\lambda_H \sim 12$–20 km (i.e., 12–20 δx, indicating that the waves are well resolved).

[33] In Figure 8, we show the cross section of the vertical velocity along the black line of Figure 7b at 2330 UTC. Vertically propagating gravity waves emitted by the wall cloud are seen on the flanks of the core with a larger amplitude on the upshear side of the storm, consistently with previous remarks. Above the core, the phase lines are nearly verti-

Table 4. Characteristics of the Dominant Mode From the Balloon Data and the Simulation

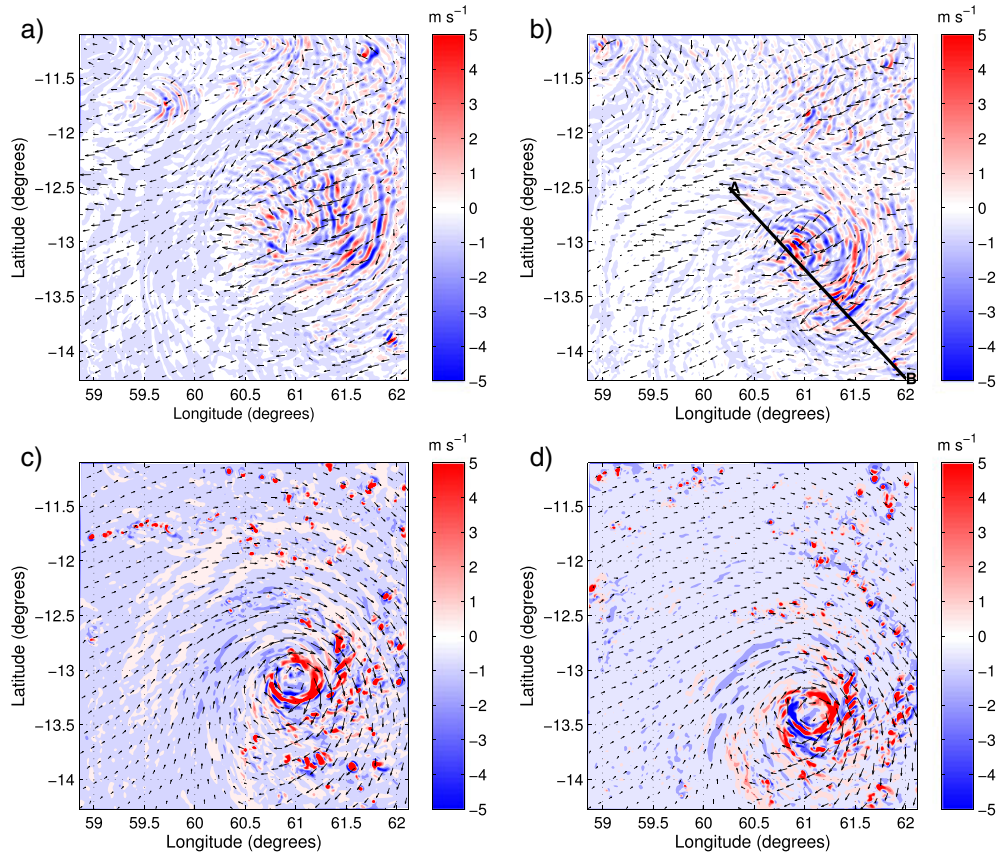|	Balloon Observations	Numerical Simulation
λ_H (km)	1	6
ω	0.2 N	0.5 N
T (min)	16	7
c (m s^{-1})	1	14

Figure 7. Vertical velocity (filled contours) and horizontal velocity vector (a) at 2030 UTC at 19 km of altitude and (c) at z = 7 km with overlaid reflectivity contour at 25 dBZ (black line). (b and d) Same as Figures 7a and 7c represented at 2210 UTC. The AB oriented line shows the slice used in subsequent figure.

cal. Those waves appear vertically trapped, and they do not carry much momentum flux vertically. As highlighted by *Lane and Knievel* [2005], increasing the resolution favors the appearance of phase lines on the flanks that are nearly vertical, indicating trapped waves. We estimate the vertical wavelength to be ~ 10 km. Using the dispersion relation for the gravity waves [*Fritts and Alexander*, 2003] and using the same previous mean value of N in the lower stratosphere above the storm yields $\hat{\omega} \sim N/\sqrt{2}$, equivalent to an intrinsic period as short as ~ 6 min.

[34] We also provide an estimation of the amplitude of the wind perturbations from the simulated field. We find $|\tilde{w}| \sim 2 - 3$ m s^{-1} at 19 km above ground level (AGL). Similarly, we get $|\tilde{u}| \sim 2$–4 m s^{-1} and $|\tilde{v}| \sim 2$–4 m s^{-1} for the horizontal zonal and meridional velocity perturbations. Those values are consistent with direct graphical estimations from the balloon time series and with a high-frequency wave.

4.2.2. Momentum Fluxes in the Simulation

[35] We have seen that the basic gravity wave characteristics derived from the numerical simulation are in agreement with those assessed from the balloon data. In the following paragraph, we carry out a more systematic calculation and comparison of the momentum fluxes from the model outputs to compare them with the momentum fluxes calculated in section 4.1.2.

[36] The momentum fluxes are calculated from the model outputs in a similar manner as in Plougonven et al. (submitted manuscript, 2012). The total wind components and the air density are interpolated at $z = 19$ km for
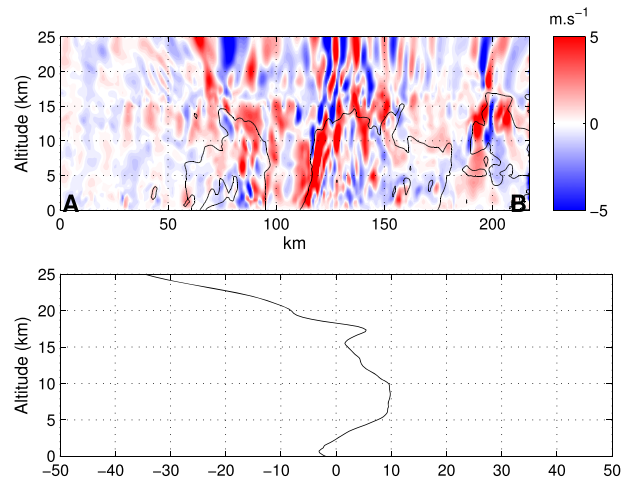

Figure 8. (top) Vertical cross section of vertical velocity (shaded contours) and reflectivity contour at 25 dBZ (black contour) along the black line on Figure 7b. (bottom) Vertical profile of the zonal velocity averaged along the vertical slice.
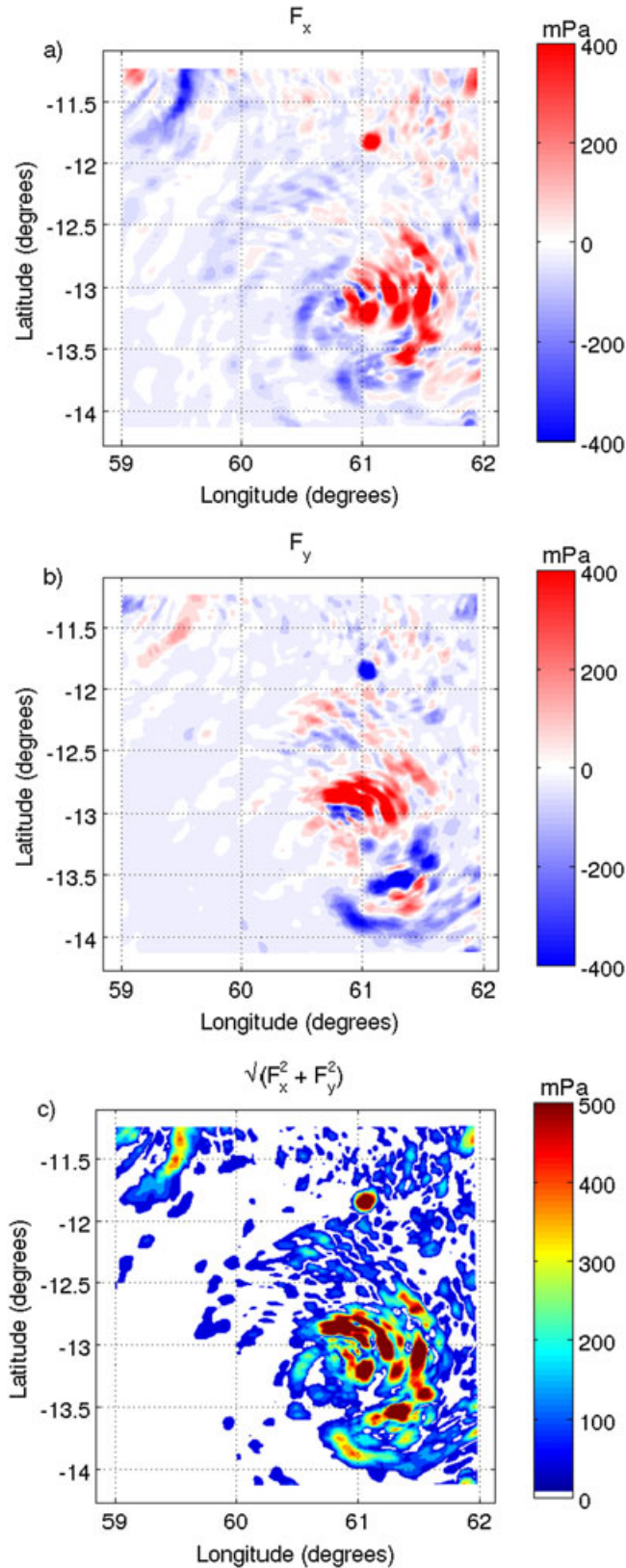
Figure 9. (a) Zonal, (b) meridional, and (c) absolute momentum fluxes in the numerical simulations on 15 February 2010, 2210 UTC, at 19 km.

comparison with the balloon. Then the wind perturbations fields are obtained at each output time step by removing the mean value over D04. We have tested removing a more local definition of the mean wind (e.g., with a 25 km averaging window). The resulting momentum fluxes are somewhat weaker and more localized. The amplitude and location of the maximum fluxes remain the same. Hence, we have preferred to keep the simplest definition for the mean flow to be removed. Zonal and meridional momentum fluxes are calculated as $\rho\, u'w'$ and $\rho\, v'w'$, respectively, and are subsequently smoothed with a 15-point averaging window.

[37] Figure 9 shows the momentum fluxes in the zonal and meridional directions calculated directly from the output velocity perturbations at 19 km AGL. The distribution of the zonal flux is highly directional as evidenced by the positive values in the eastern quadrant and the negative values mostly located on the western quadrant of the storm. The meridional distribution is also anisotropic, and the shift is parallel to the velocity vector at 19 km, as expected from the depiction of the waves in the vertical cross section.

[38] Absolute momentum flux at 19 km at 2200 UTC is represented in Figure 9c. We note that most of the momentum flux is located on the upshear side of the storm, and this is in agreement with *Sato* [1993] that stated that the maximum of the flux is on the leading side of the developing storm. This also suggests consistency with the argument of *Kuester et al.* [2008] who stated that 50% of the momentum flux emitted by a Hurricane during its lifetime is eastward flux. Our study only covers a period during the development of the cyclone; for that period, we calculate a value of 60%.

[39] In a previous case study comparing balloon-borne observations and mesoscale simulations of an orographic gravity wave, observed and simulated time series of wind and temperature along the balloon trajectory were found to agree [*Plougonven et al.*, 2008]. This was possible because the source of the wave was the orography (the Antarctic Peninsula), hence immobile and well known. For CGWs, the source of the waves is convection in the developing cyclone which, being itself simulated, unavoidably differs from the observed cyclone: we have previously seen a bias in the storm core location between the simulation and the satellite representation of convection. Hence we choose to compare the general aspect of time series from the simulations in a location comparable to that of the balloon relative to the storm core. In other words, since the balloon is located about 150–200 km north-northwesterly of the core, we illustrate the gravity waves by a local time series of momentum fluxes in D04 in a region 150–200 km north-northwesterly of the simulated core (61°E, 12°S). We have tested the sensitivity to the location chosen, within half a degree in all four directions, and have found that all time series are qualitatively similar. These time series (e.g., Figure 10) share qualitative similarities to that from the balloon data: maxima of momentum fluxes occur in short bursts (less than an hour) with about three large amplitude events in the time window analyzed, having values up to 100–250 mPa.

4.2.3. Spectral Characteristics

[40] In this section, we calculate the phase speeds and horizontal wavelengths spectra of momentum fluxes using the numerical simulation to compare them to the spectra derived from the balloon data in section 4.1.2.
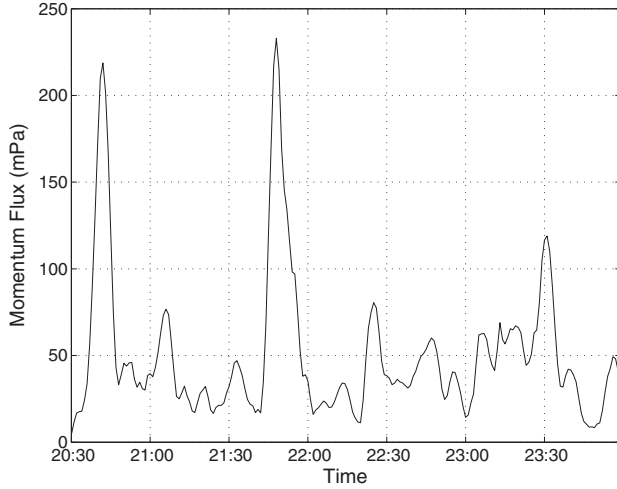
Figure 10. Time series of the momentum flux for the simulated CGWs at 61°E, 12°S.

[41] In order to perform a spectral analysis on the outputs as in *Kuester et al.* [2008], we compute the cospectra of (u', v') with w' as:

$$Co_x = Co(u'w') = \mathrm{Re}\left(UW^*\right) \qquad (11)$$

and

$$Co_y = Co(v'w') = \mathrm{Re}\left(VW^*\right), \qquad (12)$$

where (U, V, W) are the Fourier transforms of (u', v', w') and W^* is the complex conjugate of W. These 3-D (k, l, ω) cospectra are then transformed into 1-D (c or λ_H) cospectra and normalized so that they are in spectral density unit: respectively, m^2 s^{-2}/Δc and m^2 s^{-2}/$\Delta\lambda_H$. The same values as in section 4.1.2 were used, i.e., $\Delta c = 2$ m s^{-1} and $\Delta\lambda_H = 500$ m. The absolute momentum spectra are then obtained by summing the zonal and meridional components:

$$F(c) = \frac{1}{2}\bar{\rho}_0 \sqrt{Co_x(c)^2 + Co_y(c)^2} \qquad (13)$$

and

$$F(\lambda_H) = \frac{1}{2}\bar{\rho}_0 \sqrt{Co_x(\lambda_H)^2 + Co_y(\lambda_H)^2}, \qquad (14)$$

where $\bar{\rho}_0$ is the density averaged over the entire time and domain.

[42] We retrieve the mean integrated momentum flux (IMF) by integrating the latter over all the phase speeds or horizontal wavelengths:

$$\mathrm{IMF} = \int_c F(c)\mathrm{d}c = \int_{\lambda_H} F(\lambda_H)\mathrm{d}\lambda_H, \qquad (15)$$

i.e., the averaged momentum flux over the whole innermost domain (D04) throughout the developing storm period.

[43] As mentioned by *Kuester et al.* [2008], this Fourier analysis approach with the model outputs needs confirmation by verifying the consistency of the sampling rate. The Nyquist frequency should be at least twice the frequency of the highest waves frequency. Here the Nyquist frequency is approximately 0.1047 s^{-1}; therefore, the expected frequency

of the highest waves frequency should be on the order of 1–3 × 10^{-2} s^{-1}. This value corresponds to a near Brunt-Väisälä frequency, as calculated from the ECMWF reanalysis, so the chosen Nyquist frequency is appropriate to sample the high-frequency part of the spectrum of the gravity wave activity. The maximum wavelength in the simulation is constrained by the domain size (about 350 km), and the minimum wavelength (2 km) is imposed by the minimum grid spacing.

[44] For the simulations, the distributions of momentum fluxes as a function of phase speed, $F(c)$, and wavelength, $F(\lambda_H)$, are represented on Figures 5 and 6 (dashed red lines). Most of the simulated momentum flux is associated with waves with phase speeds from 5 to 50 m s^{-1}, and horizontal wavelengths between 3 and 20 km (although some signals appear up to 50 km). Waves with wavelengths from 3 to 20 km carry about two thirds of the total momentum flux. The dominant mode has a horizontal wavelength of 6 km with an intrinsic frequency of 0.5 N (period of 7 min) and a ground-relative phase speed of 14 m s^{-1}. As stated earlier, this frequency is very close to the Brunt-Väisälä frequency. The spectral characteristics of the dominant mode of the simulated gravity waves are summarized in Table 4. One should note and keep in mind that, with a grid spacing of 1 km, a wavelength of 6 km corresponds to the minimum resolved scale.

4.3. Further Comparison

[45] The sections 4.1 and 4.2 have shown a reasonable agreement between the observed and simulated CGWs during the early development of Tropical Storm Gelane. We here provide additional informations to push the comparison further, and discuss the limitations of such comparison.

[46] In Table 5, we show the values of the IMF and the standard deviation σ of the fluxes calculated from the balloon data and the numerical simulation. The IMF and the standard deviation in the observations compare fairly well with those in the numerical simulations, with an underestimation in the simulations (which can also be seen by comparing Figures 4 and 10). Actually, we do not expect a perfect match between those values because of the limitations making a precise comparison difficult: sampling of the balloon observations (very localized, in the vicinity of the storm, potential overestimation of the flux when the balloon is over the storm) and averaging domain in the simulations (which both includes the storm and quiescent regions).

[47] The momentum flux distributions estimated with the observations and simulations (Figures 5 and 6) shows encouraging similarities: both emphasize short wavelengths ($\lesssim$ 10 km) and agree regarding the importance of phase speeds between 5 and 20 m s^{-1}. However, significant discrepancies are also found. Regarding the distribution of momentum fluxes as a function of horizontal wavelength, discrepancies are found for short wavelengths ($\lesssim$ 5 km)

Table 5. Comparison of the Observed and Simulated CGWs Characteristics

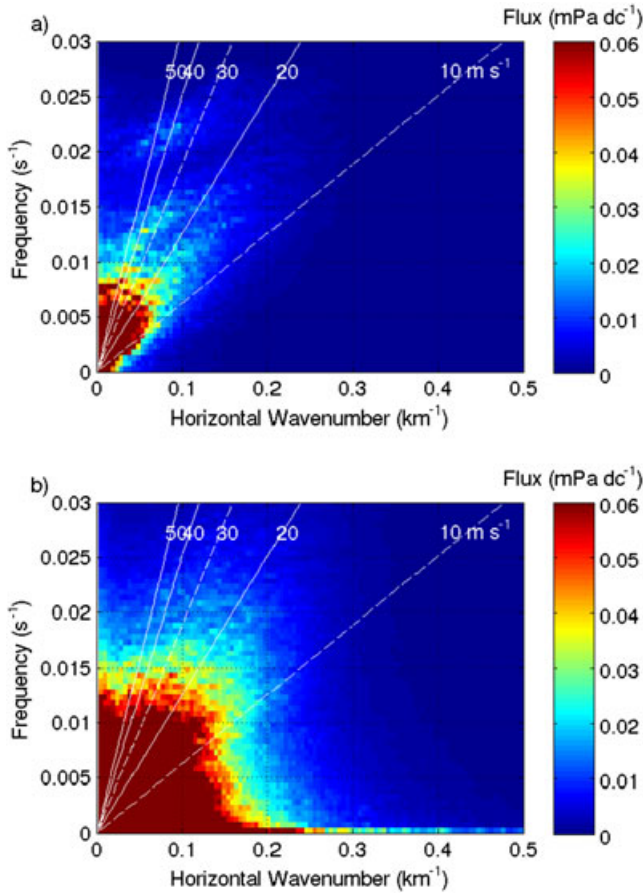|	Balloon Observations	Numerical Simulation
IMF (mPa)	133.8	89.9
Flux standard deviation (mPa)	69.4	42

Figure 11. Momentum flux with respect to frequency and horizontal wave number (a) at z = 19 km and (b) at z = 15 km.

and also for long wavelengths (isolated peaks found in the simulations, not in the observations). The latter, isolated peaks simply results from the Fourier analysis (no smoothing was applied to the Fourier transform of the WRF fields). At shorter wavelengths, one needs to compare the two curves cautiously. In the simulations, wavelengths shorter than 6 km are absent because of the limited resolution of the simulations (the minimum resolved wavelength is $\sim 6 \Delta x$). In fact, we have calculated this spectrum from the output of domain D03 (where $\Delta x = 3$ km) and have found a broader peak around 15 to 30 km. Hence, the agreement found for the peak near $\lambda_h = 6$ km may be partly fortuitous, resulting from some unresolved scales being aliased onto the minimum resolved scale. Nonetheless, both curves agree quite encouragingly down to this minimum scale, with a strong contrast between weak momentum fluxes for wavelengths larger than 15 km, and stronger values for wavelengths shorter than 15 km. The simulated fluxes are very sensitive to resolution and further investigation at higher resolution would be necessary to reach firm conclusions. More worrisome are the discrepancies in the distribution as a function of phase speeds: The observed maximum fluxes are for nearly stationary waves, whereas the simulations have nearly no momentum fluxes associated with phase speeds less than 5 m s^{-1}. This is too great a difference to be explained simply by the limited sampling of the wavefield by the balloon. (The other

differences, i.e., the simulations emphasizing larger phase speeds than the observations, can reasonably be due to the different sampling.) The absence of waves with near-zero phase speeds in the simulations suggest that these may have been filtered by the wind, which displays a reversal between 15 and 20 km (see Figure 8; wind profiles averaged over the whole domain are similar). To verify that this is indeed the case, Figure 11 displays the 2-D distribution of simulated momentum fluxes in the horizontal wavelength/frequency plane at two altitudes: 15 and 19 km. Gravity waves with near-zero phase speeds are clearly present at 15 km and constitute a significant portion of the wave field. At 19 km, on the other hand, these waves have been filtered out, and only phase speeds of about 10 m s^{-1} or larger remain. This underlines an essential difficulty in comparing high-resolution numerical simulations and observations: the mesoscale simulations rely on analyses for their initialization. However, the analyzed winds in the Tropics have larger uncertainties than in the midlatitudes, due to the paucity of tropical observations as well as the absence of a balance to relate the wind and the mass distribution (which is observed by spaceborne instruments). The simulations can therefore suffer from significant biases in the background state, which can impact the convection organization and the wave propagation in the model.

[48] We have also examined how the model resolution affects the simulated convection and the CGW momentum fluxes. For this, we compared vertical cross sections of vertical velocity and reflectivity, as well as horizontal cross sections of instantaneous momentum flux (not shown) from all three domains, D02, D03, and D04. This cannot be regarded as a "real" sensitivity test to resolution since we used two-way nesting in the simulations. Nonetheless, we notice little difference between the waves in domains 3 and 4, whereas when resolution decreases by a factor 9 (between D04 and D02), the intensity of the updrafts and the magnitude of the waves decreases by a factor 3, as well as the steepness of the phase lines. As discussed by *Lane and Knievel* [2005] and *Kim and Chun* [2010], however, the best method to retrieve GW spectral characteristics from simulations is to use the highest available resolution as the GWs are better resolved with smaller grid spacing.

4.4. Discussion

[49] We now briefly discuss two further issues for which the above analysis of CGW in both observations and simulations may be helpful: (1) Do tropical cyclones, which stand out as the most energetic form of organized convection in the troposphere, have a significant contribution to momentum fluxes toward the lower stratosphere? (2) How do the CGW generated by Gelane appear in satellite observations, which are widely used to analyze gravity waves?

[50] *Kuester et al.* [2008] have described a simple estimation of the CGW momentum flux globally associated to Hurricanes every year in the subtropical lower stratosphere. We adapt their reasoning to our case study. The calculated IMF has a value of approximately 90 mPa, about 60% of which is eastward propagating CGWs. Emphasis is put on the eastward flux here, since the eastward propagating CGWs contribute to the forcing of the positive phase of the QBO observed in February 2010. *Webster et al.* [2005] provide an estimation of a total of 475 Hurricane days per
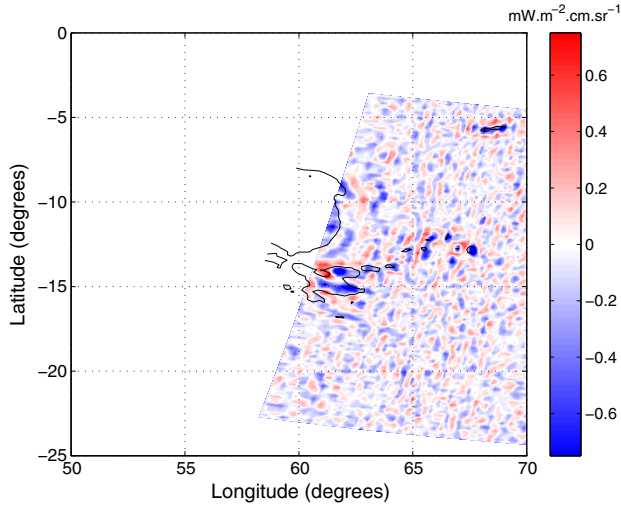
Figure 12. AIRS radiances perturbations at 2100 UTC for channel 149 on the central swath, and AIRS radiance contour at 25 m W^{-2} cm sr^{-1} (in black) to identify the deep convection regions.

year occurring across the globe. The mean zonal Tropical Cyclone momentum flux can be estimated as follows:

$$\overline{F}_{TC} = (90 \text{ mPa})0.6 \left(\frac{475 \text{ days}}{365 \text{ days}} \right) \left(\frac{3.1° \times 3.1°}{360° \times 40°} \right) \approx 4.7\,10^{-2} \text{ mPa}, \tag{16}$$

where 3.1° is the size, converted in degrees, of domain D04 over which the IMF was calculated. The factor 3.1°/40° here accounts for an equatorial band with latitude ranging from 20°S to 20°N. The above value has the same order as that mentioned in *Kuester et al.* [2008]. (In their calculation, however, they include only one geometric factor, for the longitudinal extent of the domain. Including also the latitudinal factor would reduce their estimate (5×10^{-2} mPa) by an order of magnitude.) As a matter of comparison to $\overline{F}_{TC}$, *Dunkerton* [1997] and *Scaife et al.* [2000] estimated a value of 3–6 mPa to drive the QBO. Relative to this value, the estimate for $\overline{F}_{TC}$ found above is 2 orders of magnitude smaller. Several limitations and uncertainties of this estimate should be kept in mind: the simulated IMF depends on the model configuration and on the method of calculation. We have tested and found that it is little sensitive to the spin-up time. On the other hand, it does show considerable sensitivity to resolution (60% weaker in D03 than in D04) and the IMF could increase further with higher resolution. On the other hand, the methodology we have used to estimate the momentum fluxes (use of a domain averaged mean wind) will tend to overestimate momentum fluxes. Finally, the simulated IMF compares reasonably well with the observations, but these may underestimate the momentum fluxes due to limited sampling and to the position of the balloon relative to the storm. Note also that the real flux should be higher as we have used the number of cyclone days. Now, our estimate is in fact for a developing cyclone, and previous studies have brought evidence that fluxes were larger for a developing cyclone than for a mature one. If we include Tropical Storm days, using the same value of 90 mPa yields a mean zonal momentum flux of 0.23 mPa. This remains a relatively small contribution to the momentum fluxes needed to drive

the QBO, even if we allow some room for underestimation due to resolution.

[51] The analysis of the wavefield can be qualitatively completed using satellite data, especially for the eastern part of the Storm that was not sampled by the balloon. We have previously shown AIRS radiances at channel 763 (tropospheric channel) on 15 February 2010 (Figure 2c) to reveal episodic cellular convection occurring on the upshear side of the storm. We have seen in the previous sections that such convection associated with a Tropical Storm can emit CGWs in the core and outer bands. We now show AIRS radiance perturbations on channel 149 in Figure 12 to get a planar view of the CGWs from satellite observations. They are calculated by averaging the fields along the satellite track with a 70 km running window, and removing it from the total fields. These perturbations are representative of gravity waves with vertical wavelengths greater than 12 km [*Alexander and Barnett*, 2007], and a coherent pattern of waves stands out on the eastern flank of the storm in this channel. Caution is, however, needed because the width of the channel is such that it may intercept convective storm tops. Nonetheless, in accordance with previous studies [*Gong et al.*, 2012], it appears that the gravity waves are excited preferentially by the core and the outer bands clouds as seen in the simulation. Now, the AIRS weighting function resolves only waves with large vertical wavelengths, and the filtering we used is very restrictive and filters all the spatial scales smaller than $\sim$ 70 km. Hence, although the AIRS sounding instrument provides a complementary confirmation for the structure of the emitted waves, we did not attempt in the present case to use these observations for quantitative estimates of the waves.

5. Gravity Waves in the Three PreConcordiasi Flights

[52] The case study presented in the above section has provided an example of CGWs sampled by the balloons and has allowed to assess the realism of gravity waves in mesoscale simulations of a developing cyclone. The estimate of the contribution from tropical cyclones has shown that it
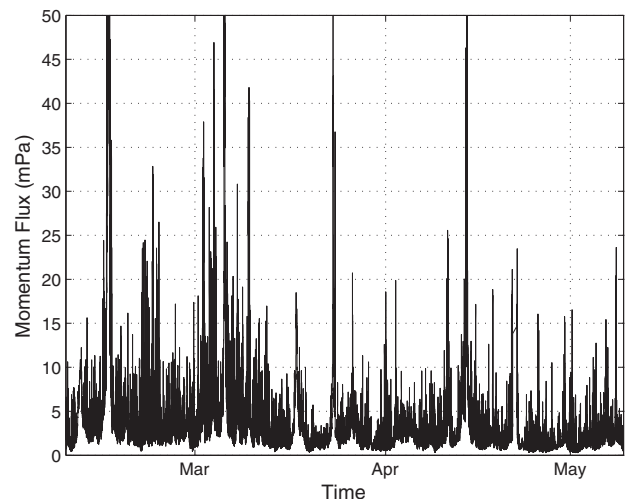

Figure 13. Momentum flux time series for the entire flight of the first PreConcordiasi balloon.

Table 6. Mean GW Momentum Flux, Momentum-Flux Weighted Averaged Phase Speeds, and Gini Coefficients for the Three PreConcordiasi Flights

Balloon #	1	2	3
IMF (mPa)	3.9	5.4	1.5
Flux standard deviation (mPa)	7.1	13.2	2.2
$\bar{c}$ (m s^{-1})	26.9	26.7	28
I_g	0.51	0.59	0.48

was necessary not to focus only on waves generated from these extreme but sparse events.

[53] In this section, making use of the whole flights of the three PreConcordiasi balloons, it is possible to analyze more generally the gravity wave field in the Tropics. We seek to characterize the CGWs and quantify their intermittency. Given the limited amount of data, we cannot derive a geographic distribution of the momentum fluxes and we restrict ourselves to the analysis of the time series.

5.1. Global Momentum Fluxes and Spectral Characteristics

[54] The momentum fluxes were analyzed from the balloon measurements using the same methodology as described in section 2.2. For illustration, we show in Figure 13 the time series of instantaneous momentum flux estimated for the entire flight of the first balloon. There are strong variations on fairly short timescales, yielding a noisy signal that is generally weaker than 10 mPa, but which contains short episodes with very intense values of several tens of mPa. As evidenced by these short and intense episodes, we observe strong GW activity in mid-February (Tropical Cyclone Gelane), throughout the month of March, and the first half of April. Table 6 summarizes different characteristics of the gravity waves observed during the flights. The comparison of the two balloons that remained in the Tropics (1 and 2, see Figure 1) shows comparable *IMF* values of about 4–5 mPa. The fact that both balloons yield comparable IMFs despite the differences in trajectories gives confidence that this value for the IMF is fairly robust, for the Tropics and for this time period. Yet, we find that the contribution of the waves with periods less than 20 min to the total momentum flux is about 40% to 50%. This suggests that those values are still sensitive to the sampling.

[55] We now review the spectral characteristics of the GWs observed by the balloons but for the entire flights. The distribution as a function of phase speed is represented in Figure 14. For Balloons 1 and 2 (black solid and dashed red), the spectra exhibit a single dominant mode with an amplitude approximately 10 times smaller than their respective counterpart in the Tropical Cyclone analysis. The momentum fluxes are integrated on a longer period of time; hence, the IMFs are reduced because the spectra results from intense CGW events such as associated with Tropical Cyclone Gelane, but also less intense convective events and weak GWs activity between two consecutive events. Although the maximum is attained for a phase speed close to zero, momentum fluxes decrease only slowly with increasing phase speed, yielding significant momentum fluxes carried by waves with phase speeds larger than 30, or even 50 m s^{-1} (about 20% of the momentum fluxes are carried by

waves with phase speeds larger than 50 m s^{-1}). Momentum flux weighted averaged phase speeds for the three balloons are found to be remarkably similar (about 27 m s^{-1}) as summarized in Table 6. The distribution for balloon #2 is slightly larger as that of balloon #1 for all phase speeds. This difference in amplitude can be explained by the fact that the second balloon observed more GW episodes as it stayed longer than balloon #1 in the Indian/West Pacific regions during intense multicellular convection. (For balloon #2, about 1 month from early April to early May 2010, versus no longer than ~ 15 days for balloon #1.) The IMFs also reflect this difference with a value for balloon #2 that is 40% higher than that of balloon #1, and a standard deviation nearly twice as large (see Table 6). The main conclusion of the comparison between the two balloons should, however, be that these differences are fairly small, relative to our uncertainty on gravity wave momentum fluxes in this region, and that the shape of the distribution is robust and well-sampled. In other words, the sampling by the two balloons yields a robust shape for the momentum flux distribution (Figure 14) and a reasonable estimate of the amplitude (to within 40%).

[56] It is interesting to discuss the differences seen in balloon #3. As can be seen in Figure 1, balloon #3 drifted away from the tropics 1 month after its launch to fly poleward then in midlatitudes, in regions where deep convection occurs less frequently. The observed GW activity in the first 10 days of the flight (not shown) corresponds to periods when the balloon flew over Africa. Only one peak of significant activity is seen by the balloon once the African continent has been totally crossed. Therefore, the momentum flux distribution of balloon #3 can be interpreted as a midlatitude distribution. The IMF is 3 to 4 times weaker than that of the "Tropical" balloons. Note that it is consistent with values found from balloon measurements and mesoscale simulations at polar latitudes (0.9 mPa) [see *Plougonven et al.*, 2013, Table 2]. Interestingly, the shape of the distribution and the average phase speed are essentially the same as for the other two balloons, further suggesting the robustness of this distribution.
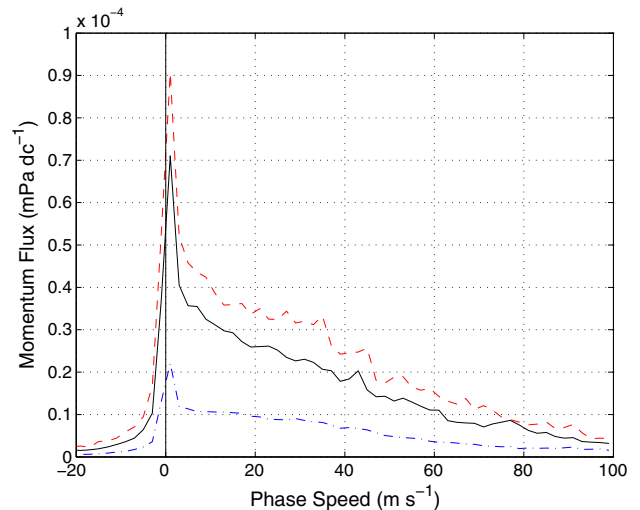

Figure 14. Same as Figure 5 for the entire flights of balloons 1 (solid black), 2 (dashed red), and 3 (strippled blue).
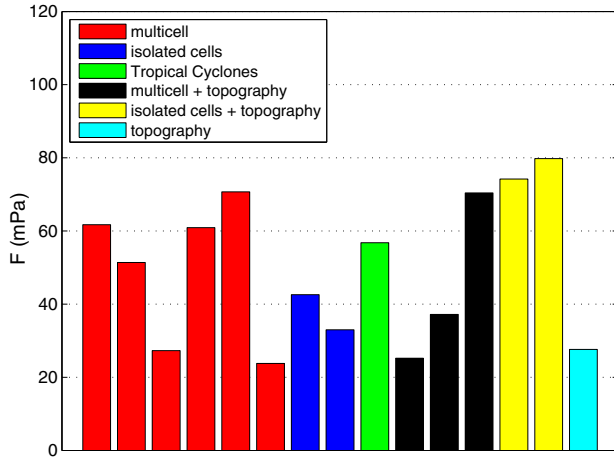
Figure 15. Convective and topographic sources of the mean GW momentum flux (greater than 20 mPa) for the three balloons. The number of bars denotes the number of a given type of event, and the height represents the mean flux during the event.

5.2. Gravity Wave Sources

[57] An important outcome of studies of gravity waves is to contribute to determine and quantify the different sources in the troposphere. At polar latitudes, *Hertzog et al.* [2008] and *Plougonven et al.* [2013] contrasted intense but very intermittent orographic sources with much weaker but more ubiquitous nonorographic sources (jets and fronts). In this section, we identify intense events (momentum fluxes larger than 20 mPa) and attempt to relate the GW to the convective or topographic environment near the balloon trajectories. We use satellite infrared radiances quick looks to determine if those episodes were associated to convection or orographic effects. When the balloons flew over or in the vicinity of convection, the event was denoted as convective, while it was marked as topographic when the balloon flew over mountains. Probable combinations of both effects were also identified. In order to get a comparison between those events in term of momentum fluxes, we have computed their associated mean flux. Those categories are summarized in Figure 15. The present observations do not suggest any conspicuous difference between the mean momentum fluxes carried by CGWs and topographic GWs. Convection appears to produce events that are as intense as orographic ones but are more frequent. We also note and emphasize that the tropical cyclone case does not stand out as a particularly intense event.

5.3. Intermittency

[58] We have seen previously that the CGW momentum fluxes vary significantly in time and space due to the sparse spatial distribution of the convective cells and the intermittency of the convective sources. As emphasized in previous studies [*Plougonven et al.*, 2008; *Hertzog et al.*, 2012], the intermittency can be quantified by momentum flux probability density functions (PDFs).

[59] Figure 16 displays the PDF of absolute momentum fluxes derived from the balloon observations. As underlined by *Hertzog et al.* [2012], PDFs exhibiting long tails account for the highly intermittent GWs in the lower stratosphere. Here they span for values up to 100 mPa for balloons #1 and #2 and 45 mPa for balloon 3. The PDFs are compared to the lognormal distribution having the same mean and standard deviation. *Hertzog et al.* [2012] have shown that over smooth terrain at high latitudes, the lognormal distribution provides a very good approximation of the PDF of momentum fluxes. We focus here on balloons #1 and #2. The lognormal distribution describes well the distribution of weak fluxes ($\lesssim$ 10 mPa) but overestimates the occurrence frequency for intermediate fluxes (10–50 mPa). At larger values (> 50 mPa), the lognormal distribution underestimates the frequency of occurrence. This suggests that strong intermittency is associated with events of convective gravity waves: as for orographic gravity waves, it is likely that the PDF deviates from the lognormal distribution by a longer tail (intense events are less rare than expected for a lognormal distribution) [*Hertzog et al.*, 2012].

[60] The long tails of the PDFs are consistent with time series of momentum flux throughout the whole flight of balloon #1 for example (Figure 13) which revealed only a few temporally localized peaks. It may be noted that the PDFs for the two first balloons compare fairly well, especially for fluxes smaller than 25 mPa. The difference for greater momentum fluxes likely arises because the sampling is insufficient to observe many rare intense events. It is thus clear that the sampling of the tropical belt by two balloons is insufficient and that further observations would be needed for the PDFs to converge.

[61] Another way to quantify the global intermittency is to compute diagnostics. Recently, *Plougonven et al.* [2013] have suggested a diagnostic used in economics to quantify inequalities of income, the Gini coefficient [*Gini*, 1912], to measure the GW intermittency. For a series of values of absolute momentum fluxes f_n, it is given by:

$$I_g = \frac{\sum\limits_{n=1}^{N-1} \left(n\bar{f} - F_n \right)}{\sum\limits_{n=1}^{N-1} n\bar{f}}, \qquad (17)$$
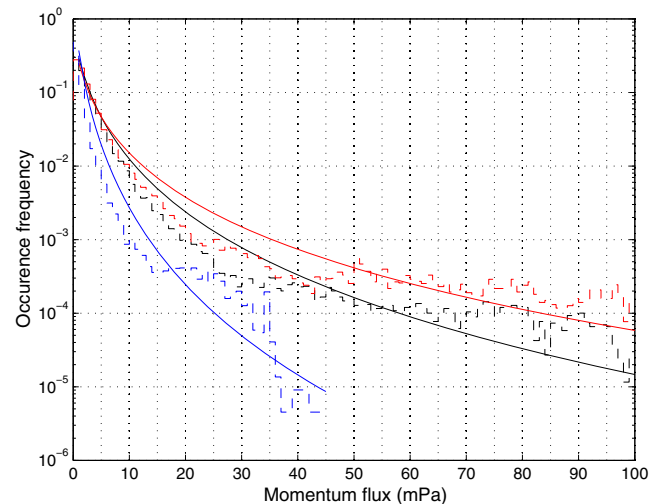

Figure 16. PDF of the momentum flux for balloons 1 (solid black), 2 (dashed red), and 3 (strippled blue).

where n represents the nth value (out of N values), $F_n = \sum_{i=1}^{n} f_i$ is the cumulative sum of the momentum fluxes f_i, and $\bar{f} = F_N/N$ is the averaged flux. A steady time series is the least intermittent series possible ($I_g = 0$) and a series with a single nonzero value is the most intermittent one ($I_g = 1$). *Plougonven et al.* [2013] argued that since this diagnostic involves summing of momentum fluxes, this method is robust to the sampling quality. We show the Gini coefficients computed for the three balloons in the last entry of Table 5. All three values are fairly close, with I_g for balloon #2 larger than the others, again reflecting the convective events from the Indian Ocean. The present results suggests that values between 0.5 and 0.6 should be expected for tropical regions, while values between 0.4 and 0.5 were typical of nonorographic regions at high latitudes and values up to 0.7 were found in regions of strong orographic gravity waves *Plougonven et al.* [2013].

6. Conclusion

[62] In situ measurements from superpressure balloons and high-resolution numerical simulations have been used to analyze gravity waves generated by convection in the Tropics. In the first part of this study, gravity waves generated by convective processes during the developing phase of the Tropical Cyclone Gelane have been analyzed and compared in balloon observations and in numerical simulations with the *Weather Research and Forecast* model. A reasonable agreement with previous numerical studies was found for the mean momentum fluxes (~ 90 mPa) and its distribution with phase speeds (main contributions associated with phase speeds in 10–40 m s^{-1}). Nevertheless, our simulations have emphasized that the major contribution to momentum fluxes was due to short horizontal wavelength (< 15 km) and short-period (< 20 min) waves.

[63] In contrast to previous studies, numerical results could here be compared to direct observations of GWs emitted by the storm. Mean momentum fluxes in the vicinity of the storm were found to be comparable and of the order of 100 mPa (for a domain of about 350 km by 350 km). The spectral analysis has shown that both observations and simulations emphasize GW with short wavelengths of 10 km or shorter. The observations suggest that it is necessary to further refine the resolution ($\Delta x = 1$ km was used in the innermost domain) in order to fully resolve the GW spectrum. Regarding phase speeds, both observations and simulations agree regarding the importance of phase speeds in the range 5–25 m s^{-1}. For larger phase speeds, larger fluxes are found in the simulations, but this could simply be due to the limited sampling of the wavefield by the balloon. A more significant disagreement is found regarding near-zero phase speeds: whereas these correspond to the largest momentum fluxes in the observations, they are nearly absent from the simulations. Analysis of the simulated wavefield at lower heights reveal that this part of the gravity wave spectrum was present a few kilometers below the flight level of the balloons but has been chopped off due to the variation of the background wind. In other words, the disagreement at near-zero phase speeds is likely due to biases in the simulation of the background wind. This illustrates how challenging it remains to precisely compare observations and mesoscale simulations

of convectively generated waves in the Tropics: the initial state and lateral boundary conditions come from analyses which are known to retain significant uncertainties, particularly at stratospheric heights and for the wind field. This contributes to making the realistic simulation of organized tropical convection a challenge, in addition to the intrinsic difficulties of simulating convection. In consequence, further case studies will be necessary to assess more precisely the realism of the simulated gravity wavefield.

[64] In the second part of this study, we have analyzed the entire time series for the three PreConcordiasi flights (February–May 2010). The two balloons that remained in the Tropics exhibit mean momentum fluxes of 3.9 and 5.4 mPa, suggesting that 5 mPa is a typical mean value for the Tropics during that time of year. However, these fluxes occur in very intermittent episodes. Fluxes were found to be concentrated during intense events with values of about 50 mPa over 1 day. Time series showed that peak values of several hundreds mPa could be reached on timescales of an hour or so. The intermittency of the gravity wavefield was quantified using PDFs and the Gini coefficient. Although sampling was insufficient to conclude, the PDFs suggest a deviation from the lognormal distribution (longer tail), as was found for regions of strong orographic GW activity [*Hertzog et al.*, 2012]. This may be partly summarized by a Gini coefficient between 0.5 and 0.6.

[65] The intense events were analyzed to identify likely sources: episodes tied to convection were found to be most frequent, but events tied to orography were also found. Both had comparable intensities. The cyclone that served as a case study did not stand out among convective events. This and an estimation based on the case study above suggests, as previous studies [*Kuester et al.*, 2008], that tropical cyclones do not have a particularly strong contribution to the overall momentum fluxes toward the Tropical stratosphere.

[66] Wavelet analysis was used to obtain the distribution of momentum fluxes as a function of phase speeds and horizontal wavelengths. Strikingly, the distribution as a function of phase speed exhibits a robust shape, with maximum fluxes for near-zero phase speeds and a slow decrease for larger phase speeds. The average phase speed was found consistently to be about 27 m s^{-1}. Besides, the contribution of waves with intrinsic periods shorter than 20 min was found to be about 40% to 50% of the total flux.

Appendix A: Effect of Depressurization Events on the Estimation of Gravity-Wave Momentum Fluxes

[67] The effect of balloon depressurization events on the momentum flux estimates can be assessed as follows. Consider a disturbance in air density (ρ') induced by a gravity wave packet, and let:

$$\zeta'_\rho = -\rho' \left(\frac{\partial \bar{\rho}}{\partial z} \right)^{-1} \qquad (A1)$$

be the associated vertical displacement of the constant-density surface. When fully pressurized, ζ'_ρ corresponds to the balloon vertical displacement [*Boccara et al.*, 2008]. This is no longer the case when the balloon is not fully inflated, as its volume V_b is free to vary, and thus its density $\rho_b = M/V_b$ with M the total mass carried by the balloon too.

[68] Now, observations show that during depressurization events, the gas temperature, which primarily results from heat exchanges by conduction with the balloon envelop, stays nearly constant. As these events occur during overcast conditions, the balloon envelop integrates radiative fluxes that do not vary much, at least away enough from the start and end of these periods. At first order, the balloon density variations can therefore be related to the helium pressure variations (P_h) with the help of the perfect gas law:

$$\frac{\delta \rho_b}{\rho_b} = \frac{\delta P_h}{P_h}. \tag{A2}$$

But, when the balloon is depressurized, $P_h \sim P$, the atmospheric pressure. Hence, when the constant-density surface is displaced upward ($\rho' < 0$), the pressure in the balloon decreases, and so the balloon density. The depressurized balloon therefore tends to amplify its vertical displacement with respect to a fully pressurized (and thus constant-volume) balloon. Assuming that the background atmosphere is in hydrostatic equilibrium, one obtains

$$\begin{aligned}\frac{\delta \rho_b}{\rho_b} &= -\frac{\bar{\rho} g}{\bar{P}} \zeta'_\rho \\ &= -\frac{g}{R\bar{T}} \zeta'_\rho. \end{aligned} \tag{A3}$$

The additional vertical balloon displacement (δz) due to this density change is therefore

$$\begin{aligned}\delta z &= \left(\frac{\partial \bar{\rho}}{\partial z}\right)^{-1} \delta \rho_b \\ &= \left(1 + \frac{R}{g} \frac{\partial T}{\partial z}\right)^{-1} \zeta'_\rho. \end{aligned} \tag{A4}$$

Hence, in the tropical lower stratosphere where $\frac{\partial T}{\partial z} > 0$, $\delta z \lesssim \zeta'_\rho$: the momentum fluxes should be overestimated by at most a factor 2 during depressurization periods.

[69] During these events, the period of the balloon neutral oscillations may also become longer than the one mentioned in section 2.2 for a pressurized balloon, and potentially exceeds the Brunt-Väisälä period. The balloon oscillations may thus be confused with gravity wave disturbances. In particular, the balloon oscillations will also be associated with wind fluctuations in the presence of wind shear. Yet gravity wave momentum fluxes are estimated from the quadrature spectrum of wind and pressure disturbances [*Boccara et al.*, 2008], whereas the balloon oscillations will tend to produce in-phase perturbations. The balloon oscillations should therefore not significantly alter the momentum flux estimations, even when the balloon is not pressurized.

References

Alexander, M. J., and C. Barnett (2007), Using satellite observations to constrain parameterizations of gravity wave effects for global models, *J. Atmos. Sci.*, *64*, 1652–1665.

Alexander, M. J. A., et al. (2010), Recent developments in gravity-wave effects in climate models and the global distribution of gravity-wave momentum flux from observations and models, *Q. J. R. Meteorol. Soc.*, *136*, 1103–1124.

Aumann, H. H., et al. (2003), AIRS/AMSU/HSB on the aqua mission: Design, science objectives, data products, and processing systems, *IEEE Trans. Geosci. Remote Sens.*, *41*, 253–264.

Austin, J., et al. (2003), Uncertainties and assessment of chemistry-climate models of the stratosphere, *Atm. Chem. Phys.*, *3*, 1–27.

Barker, D. M., W. Huang, Y.-R. Guo, and Q. N. Xiao (2004), A three-dimensional (3DVAR) data assimilation system for use with MM5: Implementation and initial results, *Mon. Weather Rev.*, *132*, 897–914.

Beres, J. H., M. J. Alexander, and J. R. Holton (2002), Effects of tropospheric wind shear on the spectrum of convectively generated gravity waves, *J. Atmos. Sci.*, *59*, 1805–1824.

Boccara, G., A. Hertzog, R. A. Vincent, and F. Vial (2008), Estimation of gravity wave momentum flux and phase speeds from quasi-Lagrangian stratospheric balloon flights. Part I: Theory and simulations, *J. Atmos. Sci.*, *65*, 3042–3055.

Butchart, N., et al. (2010), Chemistry-climate model simulations of twenty-first century stratospheric climate and circulation changes, *J. Clim.*, *23*, 5349–5374.

Chen, F., and J. Dudhia (2001), Coupling an advanced land surface hydrology model with the Penn State-NCAR MM5 modeling system. Part I: Model implementation and sensitivity, *Mon. Weather Rev.*, *129*, 569–585.

Dewan, E., R. Picard, R. O'Neil, H. Gardiner, J. Gibson, J. Mill, E. Richards, M. Kendra, and W. Gallery (1998), MSX satellite observations of thunderstormgenerated gravity waves in midwave infrared images of the upper stratosphere, *Geophys. Res. Lett.*, *25*(7), 939–942, doi:10.1029/98GL00640.

Dhaka, S., M. Takahashi, Y. Shibagaki, M. Yamanaka, and S. Fukao (2003), Gravity wave generation in the lower stratosphere due to passage of the typhoon 9426 (Orchid) observed by the MU radar at Shigaraki (34.85N, 136.10E), *J. Geophys. Res.*, *108*(D19), 4595, doi:10.1029/2003JD003489.

Dudhia, J. (1989), Numerical study of convection observed during the winter monsoon experiment using a mesoscale two-dimensional model, *J. Atmos. Sci.*, *46*, 3077–3107.

Dunkerton, T. J. (1997), The role of gravity waves in the quasi-biennial oscillation, *J. Geophys. Res.*, *102*, 26,053–26,076.

Ern, M., P. Preusse, J. C. Gille, C. L. Hepplewhite, M. G. Mlynczak, J. M. Russell III, and M. Riese (2011), Implications for atmospheric dynamics derived from global observations of gravity wave momentum flux in stratosphere and mesosphere, *J. Geophys. Res.*, *116*, D19107, doi:10.1029/2011JD015821.

Evan, S., M. J. Alexander, and J. Dudhia (2012), WRF simulations of convectively generated gravity waves in opposite QBO phases, *J. Geophys. Res.*, *117*, D12117, doi:10.1029/2011JD017302.

Fetzer, E., et al. (2003), AIRS/AMSU/HSB validation, *IEEE Trans. Geosci. Remote Sens.*, *41*, 418–431.

Fritts, D. C., and M. J. Alexander (2003), Gravity wave dynamics and effects in the middle atmosphere, *Rev. Geophys.*, *41*(1), 1003, doi:10.1029/2001RG000106.

Gentry, M. S., and G. M. Lackman (2006), The sensitivity of WRF simulations of Hurricane Ivan to the choice of cumulus parameterization, paper presented at 27th Conf. on Hurricanes and Trop. Meteor. Amer. Meteor. Soc., Monterey, CA.

Gini, C. (1912), *Variabilità e mutabilità (Variability and Mutability)*, 156 pp., Libreria Eredi Virgilio Veschi (1955), Bologna.

Gong, J., D. L. Wu, and S. D. Eckermann (2012), Gravity wave variances and propagation derived from AIRS radiances, *Atmos. Chem. Phys.*, *12*, 1701–1720.

Hertzog, A., and F. Vial (2001), A study of the dynamics of the equatorial lower stratosphere by use of ultra-long-duration balloons, 2. Gravity waves, *J. Geophys. Res.*, *106*, 22,745–22,761.

Hertzog, A., et al. (2007), Stratéole/Vorcore - Long duration, superpressure balloons to study the Antarctic stratosphere during the 2005 winter, *J. Ocean. Atmos. Tech.*, *24*, 2048–2061.

Hertzog, A., G. Boccara, R. Vincent, F. Vial, and P. Cocquerez (2008), Estimation of gravity-wave momentum fluxes and phase speeds from long-duration stratospheric balloon flights. Part II. Results from the Vorcore campaign in Antarctica, *J. Atmos. Sci.*, *65*, 3056–3070.

Hertzog, A., M. J. Alexander, and R. Plougonven (2012), On the intermittency of gravity-wave momentum flux in the stratosphere, *J. Atmos. Sci.*, *69*, 3433–3448.

Holton, J. R., P. H. Haynes, M. E. McIntyre, A. R. Douglass, R. B. Rood, and L. Pfister (1995), Stratosphere-troposphere exchange, *Rev. Geophys.*, *33*, 405–439.

Hong, S.-Y., and H.-L. Pan (1996), Nonlocal boundary layer vertical diffusion in a medium-range forecast model, *Mon. Weather Rev.*, *124*, 2322–2339.

Kain, J. S. (2004), The Kain-Fritsch convective parameterization: An update, *J. Appl. Meteorol.*, *41*, 65–98.

Kawatani, Y., S. Watanabe, K. Sato, T. J. Dunkerton, S. Miyahara, and M. Takahashi (2010), The roles of equatorial trapped waves and internal inertia-gravity waves in driving the Quasi-Biennal Oscillation. Part I: Zonal mean wave forcing, *J. Atmos. Sci.*, *67*, 963–980.

Kim, S.-Y., H.-Y. Chun, and J.-J. Baik (2005), A numerical study of gravity waves induced by convection associated with Typhoon Rusa, *Geophys. Res. Lett.*, *32*, L24816, doi:10.1029/2005GL024662.

Kim, S.-Y., H.-Y. Chun, and J.-J. Baik (2007), Sensitivity of typhoon-induced gravity waves to cumulus parameterizations, *Geophys. Res. Lett.*, *34*, L15814, doi:10.1029/2007GL030592.

Kim, Y.-J., and H.-Y. Chun (2010), Stratospheric gravity waves generated by Typhoon Saomai (2006): Numerical modeling in a moving frame following the Typhoon, *J. Atmos. Sci.*, *67*, 3617–3636.

Kim, Y.-J., S. D. Eckermann, and H.-Y. Chun (2003), An overview of the past, present and future of gravity-wave drag parametrization for numerical climate and weather prediction models, *J. Appl. Meteorol.*, *41*, 65–98.

Kuester, M. A., M. J. Alexander, and E. A. Ray (2008), A model study of gravity waves over Hurricane Humberto (2001), *J. Atmos. Sci.*, *65*, 3231–3246.

Lane, T. P., and J. C. Knievel (2005), Some effects of model resolution on simulated gravity waves generated by deep, mesoscale convection, *J. Atmos. Sci.*, *62*, 3408–3419.

Mlawer, E. J., S. J. Taubman, P. D. Brown, M. J. Iacono, and S. A. Clough (1997), Radiative transfer for inhomogeneous atmospheres: RRTM, a validated correlated-k model for the longwave, *J. Geophys. Res.*, *102*, 16,663–16,682.

Morrison, H., G. Thompson, and V. Tatarskii (2009), Impact of cloud microphysics on the development of trailing stratiform precipitation in a simulated squall line: Comparison of one- and two-moment schemes, *Mon. Weather Rev.*, *137*, 991–1007.

Nastrom, G. D. (1980), The response of superpressure balloons to gravity waves, *J. Appl. Meteorol.*, *19*, 1013–1019.

Pawson, S., et al. (2000), The GCM-Reality Intercomparison Project for SPARC (GRIPS): Scientific issues and initial results, *Bull. Am. Meteorol. Soc.*, *81*, 781–796.

Pfister, L. W. P. L., S. Scott, M. Loewenstein, S. Bowen, and M. Legg (1993), Mesoscale disturbances in the tropical stratosphere excited by convection: Observations and effects on the stratospheric momentum budget, *J. Atmos. Sci.*, *50*(D5), 1058–1075.

Plougonven, R., A. Hertzog, and H. Teitelbaum (2008), Observations and simulations of a large-amplitude mountain wave breaking above the Antarctic Peninsula, *J. Geophys. Res.*, *113*, D16113, doi:10.1029/2007JD009739.

Plougonven, R., A. Hertzog, and L. Guez (2013), Gravity waves over Antarctica and the Southern Ocean: Consistent momentum fluxes in mesoscale simulations and stratospheric balloon observations, *Q. J. R. Meteorol. Soc.*, *139*, 101–118, doi:10.1002/qj.1965.

Plu, M. (2011), A new assessment of the predictability of tropical cyclone tracks, *Mon. Weather Rev.*, *11*, 3600–3608.

Rabier, F., et al. (2010), The Concordiasi project in Antarctica, *Bull. Am. Meteorol. Soc.*, *91*(1), 69–86.

Sato, K. (1993), Small-scale wind disturbances observed by the MU radar during the passage of Typhoon Kelly, *J. Atmos. Sci.*, *50*, 518–537.

Scaife, A. A., N. Butchart, C. D. Warner, D. Stainforth, W. Norton, and J. Austin (2000), Realistic quasi-biennal oscillations in a simulation of the global climate, *Geophys. Res. Lett.*, *27*, 3481–3484.

Singh, R., P. K. Pal, C. M. Kishtawal, and P. C. Joshi (2005), Impact of bogus vortex for track and intensity prediction of Tropical Cyclone, *J. Earth Syst. Sci.*, *114*, 427–436.

Skamarock, W. C., J. B. Klemp, J. Dudhia, D. O. Gill, D. M. Barker, W. Wang, and J. G. Powers (2005), A description of the Advanced Research WRF Version 2, *Tech. Note NCAR/TN-468+STR*, Natl. Cent. for Atmos. Res., Boulder, Colo.

Skamarock, W. C., J. B. Klemp, J. Dudhia, D. O. Gill, D. M. Barker, M. G. Duda, X.-Y. Huang, W. Wang, and J. G. Powers (2008), A description of the Advanced Research WRF Version 3, *Tech. Rep.*, Natl. Cent. for Atmos. Res., Boulder, Colo.

Vincent, R. A., A. Hertzog, G. Boccara, and F. Vial (2007), Quasi-Lagrangian superpressure balloon measurements of gravity-wave momentum fluxes in the polar stratosphere of both hemispheres, *Geophys. Res. Lett.*, *34*, L19804, doi:10.1029/2007GL031072.

Wang, L. M., M. J. Alexander, P. T. Bui, and M. J. Mahoney (2006), Small-scale gravity waves in ER-2 MMS/MTP wind and temperature measurements during CRYSTAL-FACE, *Atmos. Chem. Phys.*, *6*, 1091–1104.

Webster, P. J., G. J. Holland, J. A. Curry, and H.-R. Chang (2005), Changes in tropical cyclone number, duration, and intensity in a warming environment, *Science*, *309*, 1844–1846.

Wicker, L. J., and W. C. Skamarock (2002), Time splitting methods for elastic models using forward time schemes, *Mon. Weather Rev.*, *130*, 2088–2097.